Highly Efficient Inverse Design of Semiconductor Optical Amplifiers Based on Neural Network Improved Particle Swarm Optimization Algorithm

Ting Zhao ⓘ, Wei Ji ⓘ, Pengcheng Liu ⓘ, Feng Gao ⓘ, Changpeng Li, Yiming Wang ⓘ, and Weiping Huang

Abstract—An artificial intelligent neural network improved particle swarm optimization algorithm is proposed for the inverse design of semiconductor optical amplifier. Seven input parameters, current-gain curve and saturation output power curve are selected to form the data set based on the physical model of semiconductor optical amplifier. The effectiveness of forecasting performance is improved by contrasting two back propagation neural network techniques (Scaled Conjugate Gradient and Levenberg-Marquardt) and operational settings (Central Processing Unit and Graphics Processing Unit). Higher accuracy is achieved through feedback analysis of neuron number optimization and test error. The addition of a unique backpropagation neural network can make the fitness of particle swarm algorithm mostly converge below 2×10^{-4}. The relative difference between original performances and inverse predictions is close to 0%, which proves the effectiveness of parameter extraction. This method can take advantage of neural networks to improve accuracy and speed of particle swarm optimization algorithms for efficient semiconductor optical amplifier inverse design and multi-solution analysis.

Index Terms—Particle swarm optimization, semiconductor optical amplifier, inverse design, multi-solution analysis.

I. INTRODUCTION

RECENTLY, the application of Photonic Integrated Circuit (PIC) has grown significantly [1], which has propelled many advances in data center [2], modern gas sensing [3], and photonic quantum information processing [4]. Semiconductor optical amplifier (SOA) is crucial integrated optoelectronic active device, which is widely studied as a line amplifier [5], preamplifier and compensating power amplifier [6], [7], [8]. The gain, output power and other characteristic parameters of SOA can be calculated using a set of physical models that describe the optoelectronic processes. To address the limitations of forward design, reverse structural design methods have been developed. Traditional inverse design methods for optoelectronic devices include: genetic algorithm [9], [10], gradient descent algorithm [11], [12], [13] and simulated annealing method [14]. These methods require sufficient theoretical knowledge to build simulation models, complex numerical solution: finite difference [15], alternating distribution and transfer matrix [16] and so on.

With the development of machine learning, using deep neural networks can reveal implicit input-output relationships to effectively facilitate photon prediction and inverse design [17] in a data-driven manner. In forward predictive design, artificial neural networks are applied to simulate optical processes [18], analyse response feasibility [19], 2D 3D structure prediction [20], [21] and more. For inverse structure design, tandem neural networks [22], [23], [24] have been used to design multilayer films based on target transmission spectra and also conventional nanophotonics structures.The combination of neural networks and PSO [17], [25] has been used in the reverse design of lasers, but it is limited accuracy and time-consuming. Back Propagation Neural Network (BPNN) can achieve accurate predictions, combination BPNN and particle swarm optimization (PSO) algorithms benefit to speed up computational efficiency, save the time cost of training inverse networks and achieve faster extraction of compact model parameters.

For the first time, we offer a model for SOA in this research that combines PSO algorithms with artificial intelligent neural networks. This model can automatically extract parameters based on the curve of the tested SOA performance, thus greatly enhancing the effectiveness of SOA on demand design. The second and third portions demonstrate forward prediction and inverse design. The conclusion is presented in the end.

II. FORWARD DESIGN

Utilizing forward design techniques, a more compact design model can be achieved for SOAs, making them even more attractive for various applications. The forward design data set is based on a physical model (traveling wave model) that describes the photoelectric process within the SOA. The traveling wave model [16], [26], [27], [28], [29], [30], which combines the optical wave equations, the photon density equation, and the carrier rate equation, is widely used in semiconductor active

The authors are with the School of Information Science, Engineering, Shandong University, Qingdao, Shandong 266237, China (e-mail: 202112671@mail.sdu.edu.cn; jiwww@sdu.edu.cn; 201912464@mail.sdu.edu.cn; gaofeng11@sdu.edu.cn; lichangpeng@mail.sdu.edu.cn; 202112667@mail.sdu.edu.cn; wphuang_canada@hotmail.com).
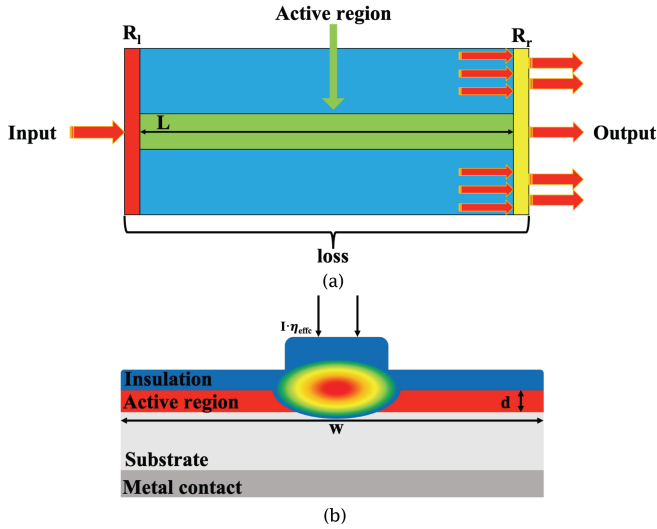
Fig. 1. (a) Top view of SOA structure;(b) Cross-sectional view of SOA structure.

device simulation and has been demonstrated to provide an accurate simulation of the SOA. Further details regarding the model can be found in the appendix. A simple schematic of SOA is shown in Fig. 1.

In order to extract the characteristic parameters of SOA, an artificial intelligent neural network for the high-precision prediction is constructed. Seven important parameters are selected from the physical model of the SOA, involving structural parameters and material coefficients; they are injection efficiency η_{effc} (dimensionless), forward reflectance R_1 (dimensionless), backward reflectance R_r (dimensionless), cavity $loss$ (in unit of cm^{-1}), optical field limiting factor Γ (dimensionless), active area thickness d (in unit of μm) and active area width w (in unit of μm). These parameters, though specific, can be generalized to other situations. They have been selected empirically with a focus on design aspects and they have a large impact on the performance of design-on-demand SOA. d and w are parameters most often considered in the design of SOA (cavity length is generally fixed integers: 300 μm, 500 μm and 1000 μm), Γ and $loss$ are parameters that will definitely influence the device, R_1 and R_r are parameters that will inevitably cause deviations in the process (try to get as close to zero as possible) and η_{effc} is the parameter that will influence the experiment. The values of the parameters are taken randomly within each specified range as $\eta_{\text{effc}} = [0.6, 1]; R_l = [0, 6e-3]; R_r = [0, 6e-3]; loss = [2e-3, 3.5e-3]; \Gamma = [0.025, 0.3]; d = [0.1, 0.2]; w = [1.5, 3]$, for a total of 10,000 different samples/combinations. The associated characteristic curves are computed using the physical model. The G-I and saturated output power curves are important static characteristics of SOA and are commonly used to analyze SOA performance. At bias currents of 350 mA and 500 mA, with input power going from −34 dBm to 15 dBm, saturation output power curves (input power vs. gain curve, input power vs. output power curve) are obtained. Current-gain curves (G-I) are obtained from 40 mA to 514 mA at an input power of −20 dBm.

TABLE I
LEVENBERG-MARQUARDT VERSUS SCALED CONJUGATE GRADIENT

Training	Neurons	Time(s)	MSE (training)	MSE (testing)
LM	9	269:32:10	0.000403	0.020162974
SCG	9	0:02:14	0.00693	0.026865207
SCG	20	0:02:34	0.000469	0.020234785
SCG	50	0:03:51	0.000233	0.020086206

The network is constructed using Scaled Conjugate Gradient (SCG) of the conjugate gradient algorithm, which performs well on a wide variety of problems, especially for networks with a large number of weights. For large-scale networks, the SCG algorithm is faster than the Levenberg-Marquardt (LM) algorithm for function approximation problems and has relatively modest memory requirements. From the Table I, SCG has a slightly lower mean square errors (MSE, i.e., difference between the NN predicted curves ($\hat{Y}_i$) and the SOA physical model calculated ones (Y_i), shown in (1)) than LM trained and tested with the same neurons, but SCG can achieve approximately the same accuracy or even ex ceed the performance of the LM algorithm when the number of neurons is increased. The application of SCG-BP neural networks allows for faster prediction and extraction of parameters.

$$\text{MSE} = \frac{1}{n} \sum_{i=1}^{n} (Y_i - \hat{Y}_i)^2 \qquad (1)$$

The designed network is connected by three hidden layers with seven input parameters as described above. According to Fig. 2, output parameters are as follows: a G-I curve with 80 data, two saturation output power curves with 100 data each, for a total of 280 output data. It is important to note that before the relevant data sets are stored in the database for neural network training, they underwent a mean normalization operation to lessen the weight imbalance of the magnitude disparities between the output data.

The training set consists of the first 9,500 data sets in the total data set of 10,000, the hidden layer contains three layers (which guarantees that complex feature parameters can be learned, because too few will result in underfitting and in reverse will result in overfitting), and the test data set consists of the last 500 data sets in the total data set. In training a forward neural network, the allocation of the training set, validation set, and test set is 70%, 15%, and 15%, respectively. The dependence of the neural network on the number of neurons is examined in order to choose the right neurons to construct the neural network topology, as shown in Fig. 3, the MSE and the time taken to predict the G-I and saturation output power curves are calculated for neural networks with different numbers of neurons. It can be seen that the test MSE does not change much after 20 neurons and has good results with lower training error and shorter time at 52 neurons.

With 52 neurons per layer, comparing the performance of the Graphic Processing Unit (GPU) and Central Processing Unit (CPU) with the same algorithm training the neural network, as shown in Fig. 4, the CPU use shorter time with a small amount of data, at the amount of data larger than 4000, the GPU training
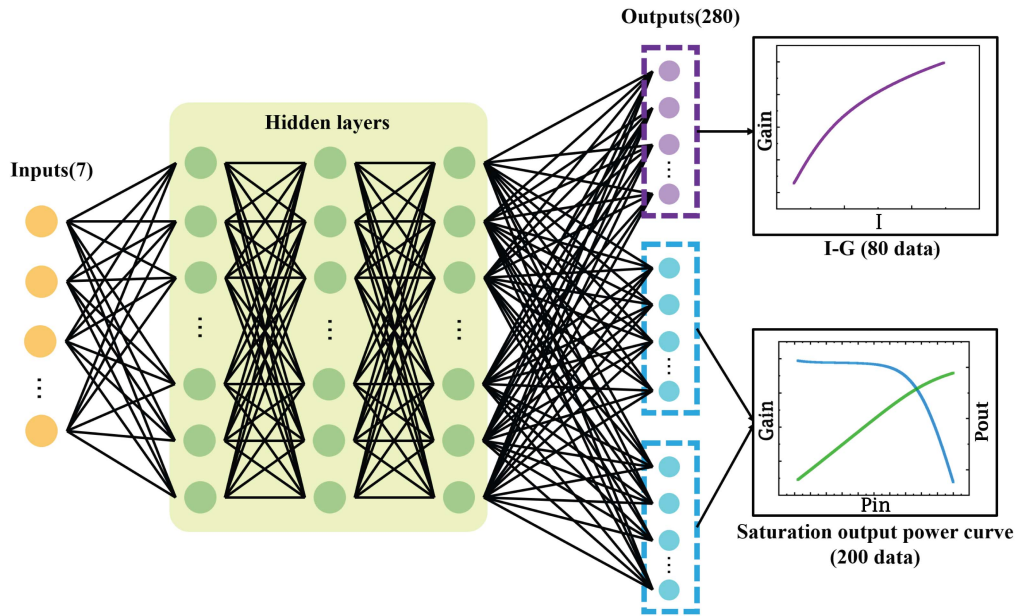
Fig. 2. The topology of forward NN with 7 input parameters and 280 output ports. The 7 inputs are the design parameters, while the 280 outputs represent the 80 G-I and the 200 saturation output power curves, respectively.
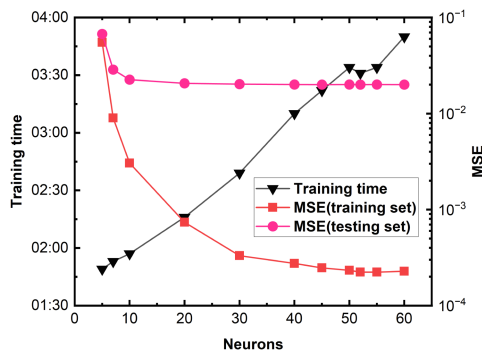

Fig. 3. The training curve and training time of the neural network according to MSE of different number of neurons, where 52 neurons are better trained.

time is shorter while the training error and testing error are similar to the CPU.

To further validate the predictive capability of the designed network, the performance of the neural network is tested by taking three sets of sample data randomly from a test dataset (different from the training dataset) of 500 sets (the network prediction data is compared with the physical model calculation data) and the results are shown in the Fig. 5.

It could be seen that the designed neural network can predict SOA performance parameters with high accuracy, extracting non-linear relationships between multiple parameters and the corresponding outputs.

The physical model takes 14049.816 seconds to calculate 500 sets of data (one G-I curve, the saturated output curve at a bias current of 350 mA and 500 mA), however, the neural network simulates 500 sets of data in 0.362 seconds, 38812 times faster, enabling faster parameter extraction.

III. INVERSE DESIGN

For the inverse design of extracting the non-linear parameters of SOA, the parallel algorithm PSO can be used to find local and global optimal solutions [31], [32]. BPNN is used to optimise the PSO algorithm (BP-PSO) so that it iterates more rapidly while maintaining high accuracy. Moreover, it avoids the phenomenon of a single solution of the cascaded network and enables the search of multiple solutions. Researchers can choose the appropriate solution according to the process capability.

The flowchart and iterative process for BP-PSO are shown in Fig. 6. The first step is initialisation: set the number of particles, the number of iterations, the acceleration factor, and set the boundary range of the algorithm; the second step is data generation: the PSO algorithm randomly generates parameters within the given range; the third step is selection of fitness: the initial fitness of each particle is calculated using the mean square error function of the neural network prediction output curve combined with the PSO algorithm and the target curve as the fitness function; the fourth step is recording. The optimal point is selected and the local optimal p_{best} and global optimal g_{best} are recorded; the fifth step is to update the constraint: the velocity of the particle is updated according to the velocity and position update formula and the position of the particle that crosses the boundary is constrained; the sixth step is to calculate the fitness: the fitness of each particle is calculated according to the selected fitness function; the seventh step is to compare the records: each particle is compared with its historical optimal value and the better point is selected as the new local optimal p_{best} and global optimal g_{best}; the last step makes a judgement: determine whether the end condition (maximum number of iterations or minimum accuracy) can be reached, if yes, output the optimum parameters, if not, skip to step five.
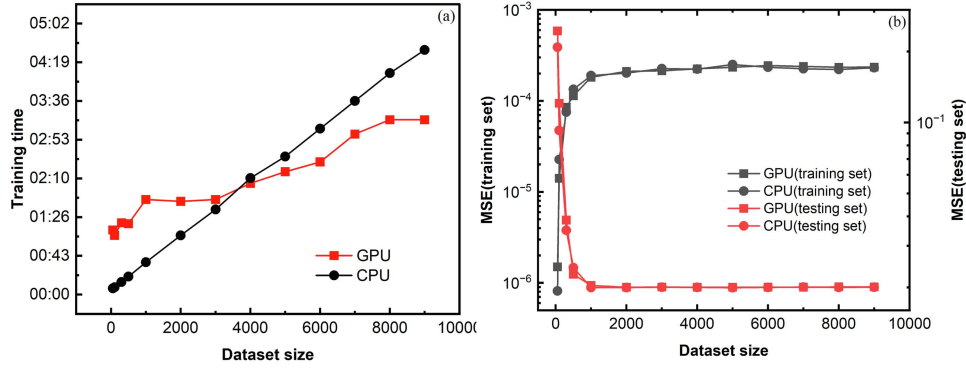
Fig. 4. Dependence of training time (a) and neural network accuracy (b) on dataset size in the CPU and GPU environments, respectively, where accuracy is expressed as MSE of the test and MSE of the training set, respectively.
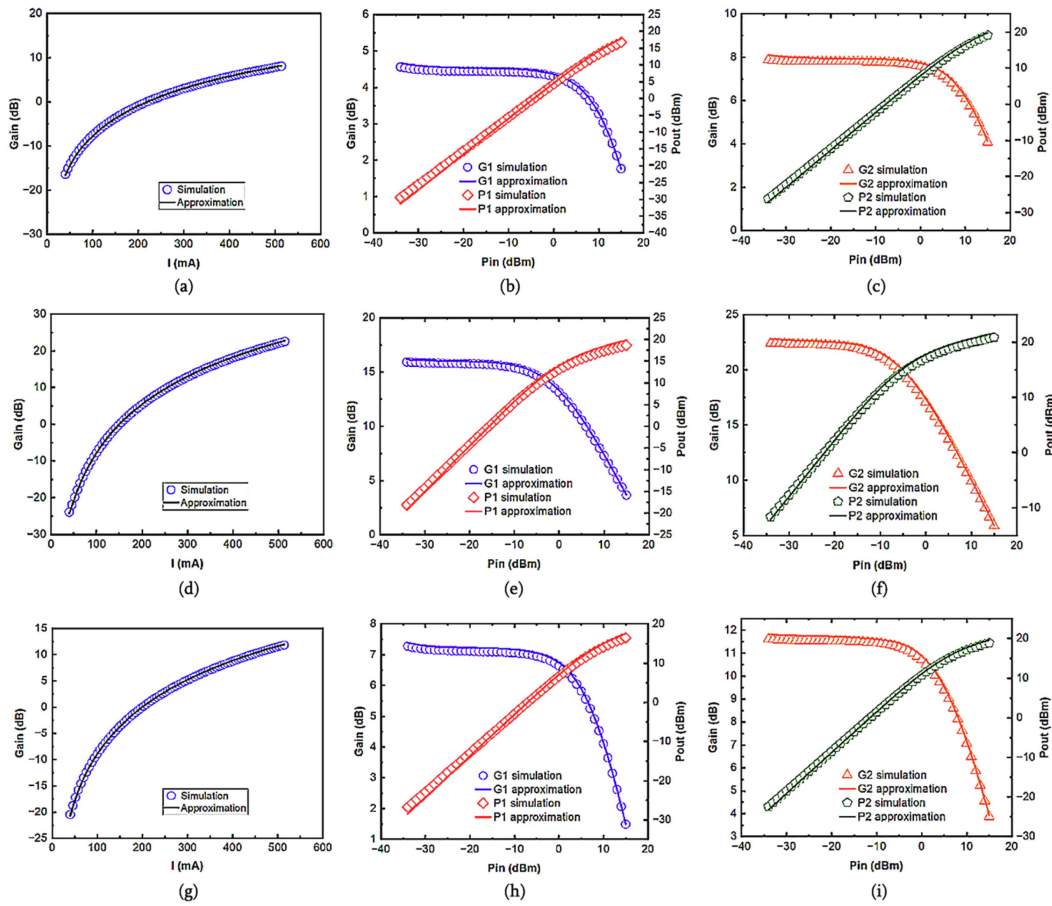

Fig. 5. (a), (d), (g) G-I, (b), (e), (h) at bias current 350 mA (G1 is the gain and P1 is the output power) and (c), (f), (i) at bias current 500 mA (G2 is the gain and P2 is the output power) saturation output power curves generated by neural network, and compared with SOA model. The saturation output power curves contain both input power-gain and input power-output power curves.

The BP-PSO search range is slightly extended from the original network training set parameters to test the robustness of the algorithm. $\eta_{\mathrm{effc}} = [0.5, 1]$; $R_l = [0, 7\mathrm{e}-3]$; $R_r = [0, 7\mathrm{e}-3]$; loss $= [1.8\mathrm{e}-3, 3.7\mathrm{e}-3]$; $\Gamma = [0.02, 0.31]$; $\mathrm{d} = [0.08, 0.22]$; $\mathrm{w} = [1.3, 3.2]$ as listed in Table II. A randomly selected set of data for BP-PSO inverse design allows multiple solutions to be obtained for analysis, i.e. a set of performance parameter curves can correspond to multiple combinations of structural design parameters, and two sets of extracted parameters are listed here for comparison with the original data.

For inverse design, the high accuracy can be verified by comparing the performance results from the predicted parameter set with the original performance parameters. Here, P1 and P2 in Table II are compared with the original data using the
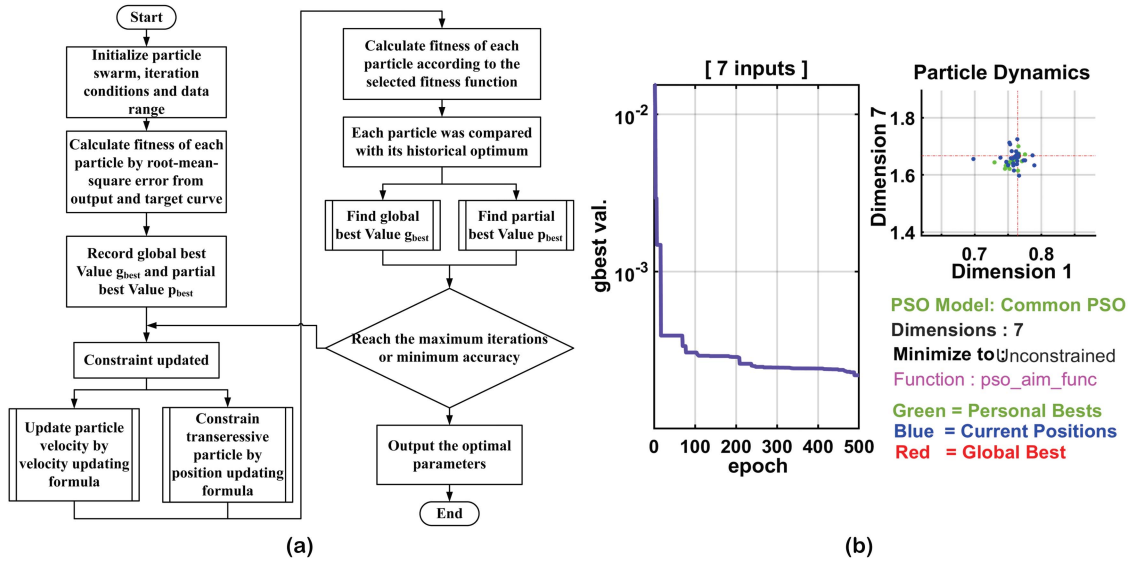
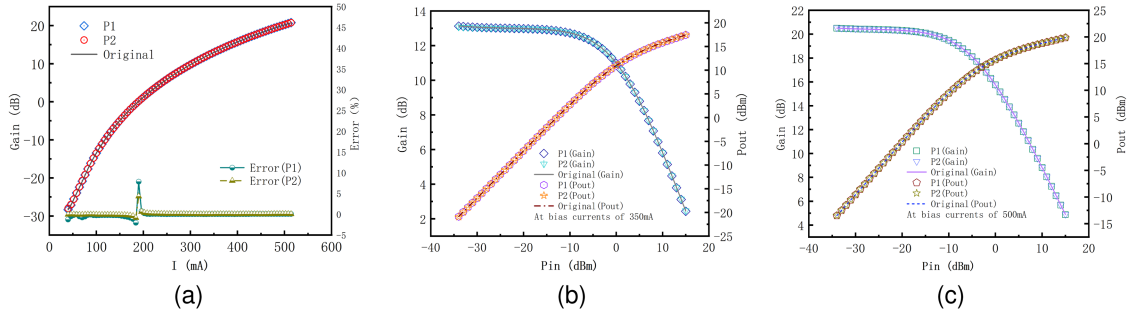Fig. 6. (a) The flow chart of BP-PSO method. (b) The convergence curve and particle dynamics diagrams.

Fig. 7. The performance of inverse design results. (a) G-I and percentage error. (b) at bias current 350 mA and (c) at bias current 500 mA saturation output power curves generated by neural network, and compared with SOA model. The saturation output power curves contain both input power-gain and input power-output power curves.

TABLE II
TWO GROUPS OF DESIGN PARAMETERS CORRESPONDING TO ONE SET OF SPECTRUM

	η_{effc}	R_l (10^{-3})	R_r (10^{-3})	$loss$ (cm^{-1})	Γ	d (μm)	w (μm)	Fitness function (10^{-4})
Original	0.7781	0.0055	0.003	0.0025	0.1436	0.1713	2.0579	–
P1	0.77753	0.00479	0.00255	0.00251	0.14363	0.12388	2.84251	1.76064
P2	0.76844	0.00414	0	0.00243	0.14353	0.16713	2.09579	1.42728
Range	0.5-1	0-7	0-7	0.0018-0.0037	0.02-0.31	0.08-0.22	1.3-3.2	–

TABLE III
MEAN AND STANDARD DEVIATION OF THE 7 PARAMETERS INVERSELY DESIGNED BY BP-PSO METHOD, AS COMPARED TO THE ORIGINAL PRESET DESIGN
PARAMETERS

	η_{effc}	R_l (10^{-3})	R_r (10^{-3})	$loss$ (cm^{-1})	Γ	d (μm)	w (μm)
Original	0.7781	0.0055	0.003	0.0025	0.1436	0.1713	2.0579
Mean	0.77273	0.00326	0.00091	0.00246	0.14357	0.15168	2.3584
STD	0.0317	1.8346	1.1437	0.0002	0.000067	0.0203	0.3275

SOA physical model to calculate curves of performance, and the results as shown in Fig. 7. The simulated performances of parameter sets predicted from the inverse predicting model are close to the target values. Moreover, Fig. 7(a) show the relative difference between original and inverse predictions in percentage. The percentage error is basically close to 0%. Overall, these results provide confidence in utilizing BP-PSO to inversely design structures of SOA.
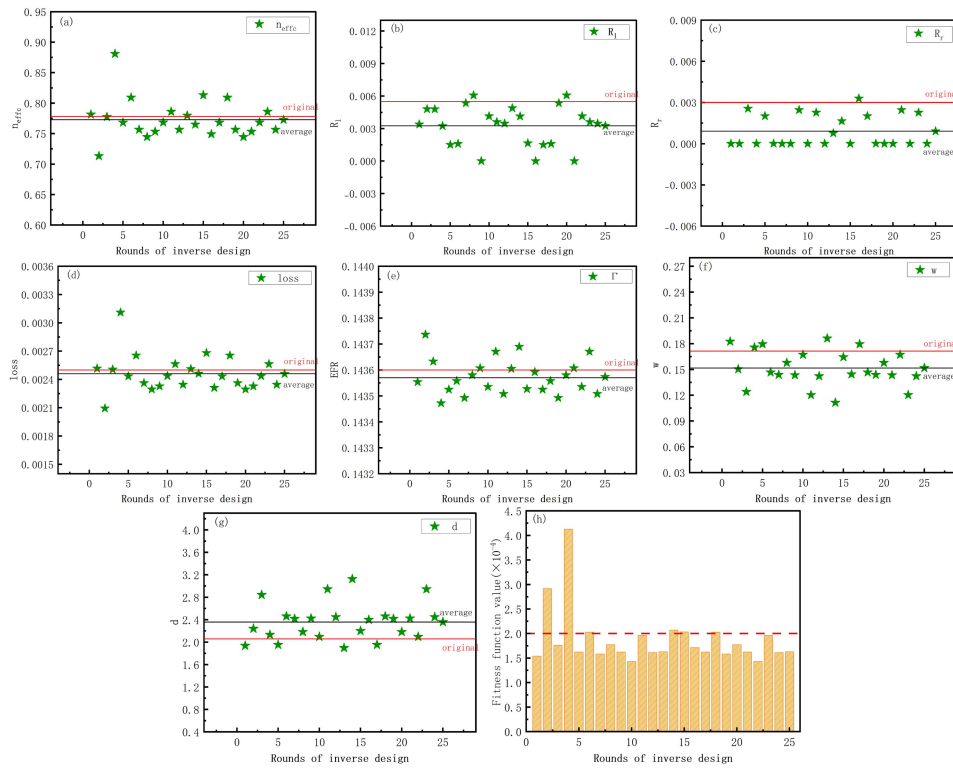
Fig. 8. (a)–(g) Statistical distribution of one randomly selected group for the inverse design parameters calculated by the BP-PSO method. The blue dots represent the parameter values generated by BP-PSO, the dashed lines represent their statistical averages and the red solid lines are the original true values; (h) the fitness function distribution of PSO at Epoch 500 for 25 repeated rounds.
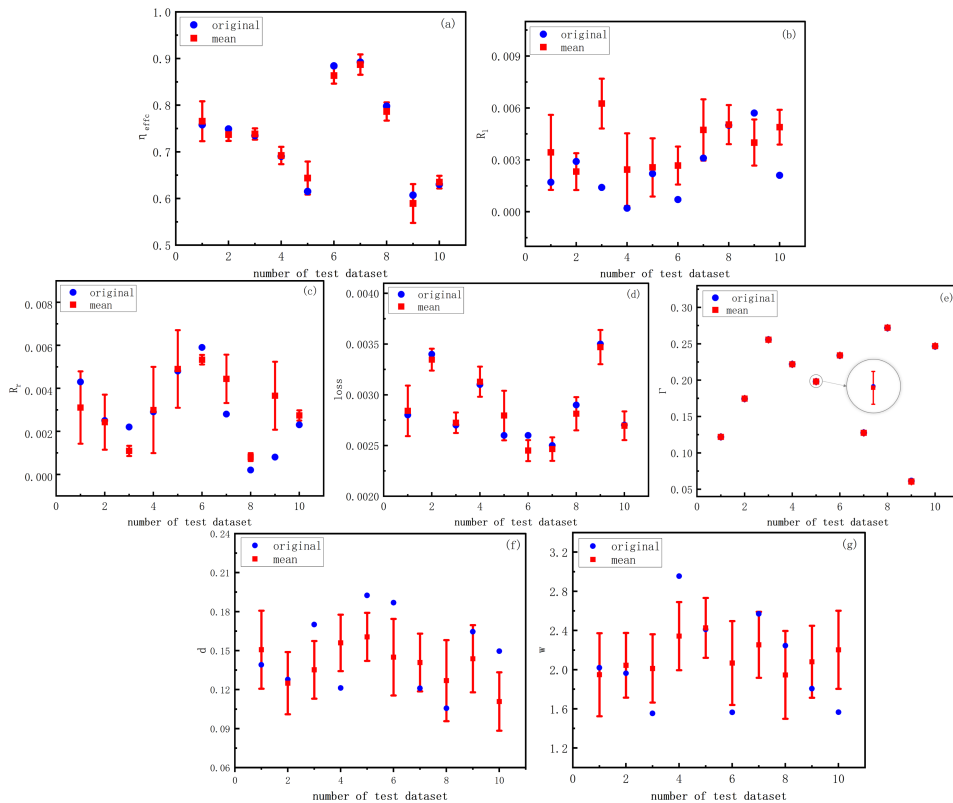

Fig. 9. (a)–(g) Mean and standard deviation of the 7 parameters inversely designed by BP-PSO method, for 10 groups of randomly data in the test dataset.

For the 25 rounds of PSO search, as shown in Fig. 8, it is indicated that the BP-PSO search is not generated aimlessly and randomly, but is distributed in a fluctuant way within a certain range of the original data. The parameters η_{effc}, $loss$ and Γ are very concentrated, and the w and d distributions are somewhat scattered, due to carrier rate equation of SOA model, where small changes in w and d are multiplied together and may cause fluctuations to the whole model. BP-PSO can be reverse designed with multiple solutions for physicality, thus providing more design possibilities for the researcher. R_l and R_r are more scattered probably from the effect of the open root sign based on the boundary conditions, and give the margin of error within which the manufacturing process can be appropriately liberalized. To clearly show the accuracy of the algorithm, the distribution of fitness function is plotted, and most of 25 times that the rounds of repeated search are performed below 2×10^{-4}, which also shows that high precision inverse design parameters can be automatically obtained by the BP-PSO algorithm. Compared to 2×10^{-3} accuracy of NN-PSO [17], one order of magnitudes higher accuracy of inverse design is presented. Their standard deviation (STD) and mean values are listed in Table III, demonstrating that there is no need to manually adjust the tested-out parameters, and that valid device parameters can be extracted in a short time by BP-PSO to solve the non-linearity problem of multiple solutions in SOA.

The means and standard deviations of ten randomly listed test datasets are used to further validate the accuracy and ability of BP-PSO algorithm to reverse-extract parameters for different datasets by reverse design, as shown in the Fig. 9. The figure shows that the reverse search designed the mean of seven parameters with standard deviation bars, and when compared with the corresponding original data (red circles), the parameters η_{effc}, $loss$ and Γ are predicted more accurately, and the remaining parameters are scattered accordingly, but the parameter of reverse extraction is still valuable for reference.

IV. CONCLUSION

The optimized PSO algorithm based on Scaled Conjugate Gradient back-propagation neural network is proposed for the inverse design of SOA to achieve parameter extraction of multiple solutions with high accuracy and computational speed. Comparing the Scaled Conjugate Gradient and Levenberg-Marquardt algorithms, the influence of GPU and CPU environments on neural networks, SCG algorithm is selected to train back-propagation neural networks in GPU environment. The neuron-dependence of the neural network (7 inputs and 280 outputs) shows that 52 neurons per hidden layer obtains the most appropriate MSE of training and testing. The reliability of the algorithm for the prediction of the G-I curve and saturated output power curve is confirmed by the performance parameters extraction based on the SOA traveling wave model. In the reverse design of SOA, the fitness of BP-PSO mostly converges to below 2×10^{-4}, which proves the effectiveness of parameter extraction. By comparing the mean and standard deviation of 10 test data sets, the effectiveness of parameter extraction in reverse design of BP-PSO is verified.

APPENDIX
PHYSICAL MODEL OF A SOA

Ridge waveguide SOA is simulated using a one-dimensional travelling wave model as shown in (A.1),

$$\left(\frac{1}{v_g}\frac{\partial}{\partial t} \pm \frac{\partial}{\partial z}\right)\begin{bmatrix} F(z,t) \\ R(z,t) \end{bmatrix} = \begin{bmatrix} G - i\delta & i\kappa \\ i\kappa^* & G - i\delta \end{bmatrix}\begin{bmatrix} F(z,t) \\ R(z,t) \end{bmatrix} + \begin{bmatrix} S_f(z,t) \\ S_r(z,t) \end{bmatrix} \quad (A.1)$$

where $F(z,t)$ and $R(z,t)$ are amplitudes of the forward and backward waves respectively, v_g is the group velocity, κ is the coefficient of mutual coupling of the forward and backward waves, G is the mode gain, δ is the detuning factor, $S_f(z,t)$ and $S_r(z,t)$ is the amplitude of the forward and backward spontaneous radiation noise respectively. The boundary conditions for (A.1) are (A.2):

$$\begin{cases} F(0,t) = \sqrt{R_l}R(0,t) + \sqrt{1 - R_l}E_s(t)e^{-j(\omega - \omega_0)t} \\ R(l,t) = \sqrt{R_r}F(l,t) \end{cases} \quad (A.2)$$

where $F(0,t)$ and $R(l,t)$ are amplitudes of the forward light field at device's start and the backward light field at its end, respectively. r_1 and r_2 are the reflectance at the first and end of the device respectively, $E_s(t)$ are complex amplitudes of the incident signal light and ω_0 are reference frequencies.

The mode gain in (A.1) can be expressed as

$$G = \frac{1}{2}\left(\Gamma g_m - \alpha\right) \quad (A.3)$$

where α is waveguide loss, g_m is material gain for bulk materials and Γ is optical field limiting factor. Γ is defined as the percentage of the overlap area of the light field with the active area in relation to the overall light field distribution. The material gain can usually be expressed by the empirical formula shown in (A.4):

$$g_m = \frac{g_p \cdot \ln\left(\frac{N}{N_0}\right)}{1 + \varepsilon P} \quad (A.4)$$

where g_p is the material differential gain, N is the carrier concentration, N_0 is the transparent carrier concentration, ε is the non-linear saturation factor of the gain, P is the photon density and can be expressed as:

$$P = \frac{\Gamma}{2\hbar\omega v_g A}\sqrt{\frac{\varepsilon_0}{\mu_0}}n_{\text{effc}}\left(|F(z,t)|^2 + |R(z,t)|^2\right) \quad (A.5)$$

where $\hbar$ is the approximate Planck constant, ω is the angular frequency, A is the cross-sectional area of the active area, n_{effc} is the material equivalent refractive index and can be expressed as:

$$n_{\text{effc}} = n_{\text{eff0}} - \frac{\lambda_0}{4\pi}\Gamma\alpha_m g_m \quad (A.6)$$

n_{eff0} is the equivalent refractive index in the absence of current injection.

The amplitude of the spontaneous radiated noise in (A.1) satisfies the Gaussian distribution, the phase satisfies the uniform distribution between 0 and 2π, and its autocorrelation function

TABLE IV
PARAMETERS USED IN MODELING

Parameters	Values
Optical carrier wavelength [nm]	1550
Length of the SOA, L [μm]	500
Effective index without injection, n_{eff0}	3.18
Group index, n_g	3.6
Non-linear gain saturation coefficient , ε $[10^{-17}$ cm$^3]$	7
Linewidth enhancement factor, α_H	4.86
Transparent carrier density, N_{tr} $[10^{18}$ cm$^{-3}]$	0.4
Linear recombination coefficient, A $[10^9$ s$^{-1}]$	10
Bimolecular radiation coefficient, B $[10^{-10}$ cm^3 s$^{-1}]$	2
Auger coefficient, C $[10^{-29}$ cm^{-6} s$^{-1}]$	5
Spontaneous emission coupling coefficient, γ	0.025
Spontaneous emission coefficient, n_{sp}	1.7
Vacuum magnetic permeability, μ_0 $[10^{-7}$H/m$]$	4π
Vacuum dielectric constant, ε_0 $[10^{-12}$ F/m$]$	8.854

is:

$$\langle S(z,t)S^*(z',t')\rangle = \beta K_{tr'}\frac{BN^2}{L}v_g\delta(z-z')\delta(t-t') \tag{A.7}$$

The carrier rate equation is used in this case to approximate the carrier variation because it has little bearing on the precise computation of the optical field distribution in SOA. The carrier production rate due to electron injection, minus the carrier rate consumed by various complexes, and the carrier rate consumed during photon generation are expressed by this equation, and is written as:

$$\frac{dN}{dt} = \frac{\eta I}{eV} - AN - BN^2 - CN^3 - v_g g_m P \tag{A.8}$$

where η is the current injection efficiency, I is the injection current, e is the amount of charge, A, B, C are the rate of linear radiative compounding, bimolecular radiative compounding, and intermittent compounding, respectively. V is the total volume of the active area, and is written as:

$$V = L \cdot w \cdot d \tag{A.9}$$

where w is the width of the active area and d is the thickness of the active area. The SOA gain is calculated as follows:

$$\text{Gain (dB)} = 10\lg\left(\frac{P_{out}}{P_{in}}\right) \tag{A.10}$$

Thus, equations (1) to (10) together form a set of physical models that describe the SOA. SOA requires a high carrier concentration to maintain high gain and large saturation power, it also requirements a small optical field limiting factor that allows the swift field of the light wave to extend into the P-type cladding. Other parameters of the SOA are shown in the Table IV.

REFERENCES

[1] N. Quack et al., "MEMS-Enabled silicon photonic integrated devices and circuits," *IEEE J. Quantum Electron.*, vol. 56, no. 1, Feb. 2020, Art. no. 8400210. [Online]. Available: https://www.webofscience.com

[2] X. Shen, B. Chen, Y. Zhu, and W. Shi, "Silicon photonic integrated circuits and its application in data center," *Proc. SPIE*, vol. 11763, 2021, Art. no. 1176380.

[3] A. Hansel and M. J. R. Heck, "Opportunities for photonic integrated circuits in optical gas sensors," *J. Phys.- Photon.*, vol. 2, no. 1, Jan. 2020, Art. no. 012002.

[4] L.-T. Feng, G.-C. Guo, and X.-F. Ren, "Progress on integrated quantum photonic sources with silicon," *Adv. Quantum Technol.*, vol. 3, no. 2, Feb. 2020, Art. no. 1900058.

[5] J. Renaudier et al., "Recent advances in 100+nm ultra-wideband fiber-optic transmission systems using semiconductor optical amplifiers," *J. Lightw. Technol.*, vol. 38, no. 5, pp. 1071–1079, Mar. 2020.

[6] S. Kono, R. Koda, H. Kawanishi, and H. Narui, "9-kW peak power and 150-fs duration blue-violet optical pulses generated by GaInN master oscillator power amplifier," *Opt. Exp.*, vol. 25, no. 13, pp. 14 926–14 934, Jun. 2017.

[7] M. Jamali, V. Ahmadi, and M. Razaghi, "Switching characteristics of SOA-based sagnac interferometer for subpicosecond pulses," in *Proc. IEEE 6th Int. Symp. Telecommun.*, 2012, pp. 728–732. [Online]. Available: https://www.webofscience.com/wos/alldb/full-record/WOS:000317974700137

[8] Z. Li, Y. Li, S. Luo, F. Yin, Y. Wang, and Y. Song, "Amplified 100 Gb/s/lambda PAM-4 TDM-PON Supporting PR-30 Power Budget with \textgreater 18 dB Dynamic Range SOA amplified 100 gb/s/lambda PAM-4 TDM-PON supporting PR-30 power budget with \textgreater 18 dB dynamic range," *Micromachines*, vol. 13, no. 3, Mar. 2022, Art. no. 342.

[9] S. F. Shu, "Evolving ultrafast laser information by a learning genetic algorithm combined with a knowledge base," *IEEE Photon. Technol. Lett.*, vol. 18, no. 2, pp. 379–381, Jan. 2006.

[10] R. S. Hegde, "Photonics inverse design: Pairing deep neural networks with evolutionary algorithms," *IEEE J. Sel. Topics Quantum Electron.*, vol. 26, no. 1, Jan./Feb. 2020, Art. no. 7700908.

[11] O. Sigmund, "Topology optimization in nano-photonics," in *Theoretical and Computational Nanophotonics*, vol. 1176, D. N. Chigrin, Ed., Melville, NY, USA: Amer. Inst. Phys., 2009, pp. 26–28. [Online]. Available: https://www.webofscience.com/wos/alldb/full-record/WOS:000280420600010

[12] A. Y. Piggott, J. Lu, K. G. Lagoudakis, J. Petykiewicz, T. M. Babinec, and J. Vuckovic, "Inverse design and demonstration of a compact and broadband on-chip wavelength demultiplexer," *Nature Photon.*, vol. 9, no. 6, Jun. 2015, Art. no. 374–+.

[13] K. Yamazoe, I. Mochi, and K. A. Goldberg, "Gradient descent algorithm applied to wavefront retrieval from through-focus images by an extreme ultraviolet microscope with partially coherent source," *J. Opt. Soc. Amer. a- Opt. Image Sci. Vis.*, vol. 31, no. 12, pp. B34–B43, Dec. 2014.

[14] S. Kirkpatrick, C. Gelatt, and M. Vecchi, "Optimization by simulated annealing," *Sci.*, vol. 220, no. 4598, pp. 671–680, 1983.

[15] Y. Li, Y. Xi, X. Li, and W.-P. Huang, "Design and analysis of single mode fabry-perot lasers with high speed modulation capability," *Opt. Exp.*, vol. 19, no. 13, pp. 12131–12140, Jun. 2011.

[16] X. Li, *Optoelectronic Devices: Design, Modeling, and Simulation*. Cambridge, U.K.; New York, USA: Cambridge Univ. Press, 2009.

[17] Z. Ma and Y. Li, "Parameter extraction and inverse design of semiconductor lasers based on the deep learning and particle swarm optimization method," *Opt. Exp.*, vol. 28, no. 15, Jul. 2020, Art. no. 21971. [Online]. Available: https://opg.optica.org/abstract.cfm?URI=oe-28-15-21971

[18] J. Peurifoy et al., "Nanophotonic particle simulation and inverse design using artificial neural networks," in *Physics and Simulation of Optoelectronic Devices Xxvi*, vol. 10526, B. Witzigmann, M. Osinski, and Y. Arakawa, Eds., Bellingham, WA, USA: SPIE-Int. Soc. Opt. Eng., 2018, Art. no. UNSP 1052607.

[19] Y. Kiarashinejad, M. Zandehshahvar, S. Abdollahramezani, O. Hemmatyar, R. Pourabolghasem, and A. Adibi, "Knowledge discovery in nanophotonics using geometric deep learning," *Adv. Intell. Syst.*, vol. 2, no. 2, Feb. 2020, Art. no. 1900132.

[20] N. Yu et al., "Light propagation with phase discontinuities: Generalized laws of reflection and refraction," *Sci.*, vol. 334, no. 6054, pp. 333–337, Oct. 2011.

[21] N. Yu and F. Capasso, "Flat optics with designer metasurfaces," *Nature Mater.*, vol. 13, no. 2, pp. 139–150, Feb. 2014.

[22] X. Xu, C. Sun, Y. Li, J. Zhao, J. Han, and W. Huang, "An improved tandem neural network for the inverse design of nanophotonics devices," *Opt. Commun.*, vol. 481, Art. no. 126513, Feb. 2021.

[23] S. So, J. Mun, and J. Rho, "Simultaneous inverse design of materials and structures via deep learning: Demonstration of dipole resonance engineering using core-shell nanoparticles," *ACS Appl. Mater. Interfaces*, vol. 11, no. 27, pp. 24 264–24 268, Jul. 2019.

[24] Y. Long, J. Ren, Y. Li, and H. Chen, "Inverse design of photonic topological state via machine learning," *Appl. Phys. Lett.*, vol. 114, no. 18, May 2019, Art. no. 181105.

[25] Z. Ma, P. Feng, and Y. Li, "Inverse design of semiconductor laser parameters based on deep learning and particle swarm optimization method," *Proc. SPIE*, vol. 11209, 2019, Art. no. 137.

[26] J. Park, X. Li, and Wei-Ping Huang, "Performance simulation and design optimization gain-clamped semiconductor optical amplifiers based on distributed bragg reflectors," *IEEE J. Quantum Electron.*, vol. 39, no. 11, pp. 1415–1423, Nov. 2003. [Online]. Available: https://ieeexplore.ieee.org/document/1242360/

[27] W. Wong and K. Blow, "Travelling-wave model of semiconductor optical amplifier based non-linear loop mirror," *Opt. Commun.*, vol. 215, no. 1, pp. 169–184, 2003. [Online]. Available: https://www.sciencedirect.com/science/article/pii/S003040180202179X

[28] A. R. Totović, J. V. Crnjanski, M. M. Krstić, and D. M. Gvozdić, "Numerical study of the small-signal modulation bandwidth of reflective and traveling-wave SOAs," *J. Lightw. Technol.*, vol. 33, no. 13, pp. 2758–2764, Jul. 2015.

[29] L. Dong et al., "Modeling widely tunable sampled-grating DBR lasers using traveling-wave model with digital filter approach," *J. Lightw. Technol.*, vol. 27, no. 15, pp. 3181–3188, Aug. 2009.

[30] I. Huynen, A. Salamone, and M. Serres, "A traveling-wave model for optimizing the bandwidth of p-i-n photodetectors in silicon-on-insulator technology," *IEEE J. Sel. Topics Quantum Electron.*, vol. 4, no. 6, pp. 953–963, Nov./Dec. 1998.

[31] K. Deep, S. Sharma, and M. Pant, "Modified parallel particle swarm optimization for global optimization using message passing interface," in *Proc. IEEE 5th Int. Conf. Bio-Inspired Comput.: Theories Appl.*, 2010, pp. 1451–1458.

[32] J. Lu, W. Hu, Y. Wang, L. Li, P. Ke, and K. Zhang, "A hybrid algorithm based on particle swarm optimization and ant colony optimization algorithm," in *Smart Computing and Communication*, M. Qiu, Ed., Cham, Switzerland: Springer, 2017, pp. 22–31.